IEEE Access
Multidisciplinary ⋮ Rapid Review ⋮ Open Access Journal

Received December 17, 2019, accepted December 25, 2019, date of publication December 30, 2019,
date of current version January 7, 2020.

Digital Object Identifier 10.1109/ACCESS.2019.2962871

Cloud Extraction Scheme for Multi-Spectral Images Using Landsat-8 OLI Images With High Brightness Reflectivity Covered

TINGTING WU[1] AND LING HAN[1,2]
[1]School of Geology Engineering and Geomatics, Chang'an University, Xi'an 710064, China
[2]Shaanxi Key Laboratory of Land Consolidation and Rehabilitation, Chang'an University, Xi'an 710064, China

Corresponding author: Ling Han (2016026027@chd.edu.cn)

This work was supported in part by the Natural Science Foundation of Shaanxi Province, China, under Grant 2017JZ009, and in part by the Project of the Open Fund for Key Laboratory of Land and Resources Degenerate and Unused Land Remediation under Grant SXDJ2017-7.

ABSTRACT Cloud extraction is a vital step in remote sensing image processing. Although many advanced cloud extraction methods have been proposed and confirmed to be effective in recent years, there are still difficulties in cloud extraction in areas of high brightness reflectivity covered. High brightness reflectivity cover can have similar spectral characteristics as clouds, and thus, it is easily confused with clouds in cloud extraction schemes. This work presents a novel scheme designed to extract clouds in satellite imagery with high brightness reflectivity covered. The fractal summation method and spatial analysis are used to extract the clouds in the Landsat 8 Operational Land Imager (OLI) images containing high brightness reflectivity covered. The scheme consists of three main steps: cloud extraction based on pixel values, Anselin Local Moran's I value, and anisotropy. Pixel values were applied to extract the clouds associated with anomalies, and the last two steps were conducted to eliminate false anomalies. The findings showed that the cloud-associated anomaly pixel-values well approximate a power-law function, but both the real and fake anomaly patches (e.g., snow/ice, desert, etc.) routinely coexist within the same (fractal) scaleless segments, and that the latter seems to be more significant than the former. Consequently, these results indicate that the diagnostic difference between true and false anomalies must lie in their spatial distribution patterns. Furthermore, experiments confirmed that the fractal dimension and spatial distribution (i.e. Anselin Local Moran's I index and anisotropy) difference between the real and false anomalies displayed a certain universality. The proposed scheme effectively reduces the confusion and misclassification caused by cloud, snow and the highlighted underlying surface. It is of great significance for cloud restoration processing, image analysis, image matching, target detection and extraction, and effective extraction and utilization of remote sensing data.

INDEX TERMS Cloud extraction, spatial information, fractal summation method, Anselin Local Moran's I, anisotropic analysis.

I. INTRODUCTION

The first step in the application of satellite remote sensing images is to select appropriate satellite images. However, not all satellite remote sensing images can meet the requirements for the intelligent application of satellite remote sensing image information. In the selection of satellite image data, cloud cover is a very important judgment index. Statistics from the International Satellite Cloud Climatology Project (ISCCP) show that, on average, 66.7% of the Earth's surface is covered by clouds. Ground objects observed by remote sensing satellites will be blocked by these clouds [1]. The presence of clouds will greatly affect the application of remote sensing satellite imagery. Cloud extraction is a crucial step in the processing of remote sensing imagery. Thick clouds cover ground objects and reduce the effective information contained in the satellite image, whereas thin clouds and the underlying surface are mixed with each other, which also changes the spectrum and texture information of the image to a certain extent, making target recognition and image analysis

The associate editor coordinating the review of this manuscript and approving it for publication was Wenming Caos.

difficult [2]–[6]. Clouds are notoriously difficult to extract in Landsat images due to the limited Landsat spectral bands and the complexity of the clouds themselves [7]. A difficulty in cloud extraction is that several objects, such as snow, ice and sand on land, are similar to clouds in satellite images. Among these objects, snow is the most typical object that is similar to clouds [8]. Some cloud extraction schemes tend to mistake snow for clouds because both targets are bright and display very similar spectral characteristics [8], [9]. An incorrect cloud assessment can lead to poor utilization of imaging resources and effort. Consequently, it is important to design accurate cloud cover extraction schemes.

A number of studies have attempted to optimize cloud extraction based on spectral characteristics. The spectral-based method mainly utilizes the spectral characteristics that clouds and other ground cover have in different bands [10]. For example, Ackerman et al. [11] determined whether a given pixel was a cloud pixel or otherwise using its values; however, it was difficult to differentiate between underlying surfaces with a reflectance similar to that of clouds using this method. Crane and Anderson discussed the discrimination of snow/cloud surfaces at near-infrared wavelengths [12] using an experimental snow/cloud discrimination sensor onboard a U.S. Air Force Defense Meteorological Satellite Program platform. Salomonson and Appel [13] and Homan *et al.* [14] made use of this contrast feature to analyze image snow cover by normalizing the snow index. This method reduced misjudgments to a considerable extent, but it is difficult to accurately determine the threshold. Previous pixel-based classifiers have been developed for remote sensing instruments using machine learning techniques, for example artificial neural networks (ANNs) [3], [15]–[17], and they have achieved good results in cloud extraction [18]. ANNs have been added to remote sensing Environment for Visualizing Images (ENVI). Back propagation (BP) neural network algorithm is applied to ENVI software. However, their computational costs are very expensive and the convergence speed is slow [19]. A new cirrus band (Band 9) has been added to the Landsat 8 satellite to extract clouds, which resulted in an effective method for extracting clouds contamination. However, this method is restricted by the land cover background compared with most algorithms that are influenced by high brightness values, such as from snow or a desert [20].

Texture features are taken into account to describe the differences among different types of ice-snow surfaces and clouds. Usually, texture is defined as the arrangement of the elements with different sizes and shapes composing an image [21]. This method does not need to consider the spectral signal difference and band design between different satellite sensors [22]. Texture features based on the support vector machine (SVM) scheme have been used to extract the clouds in satellite images of ice-snow areas, and the experimental results indicate that this scheme performs well, especially for thin cirrus clouds. However, inevitably, textures are difficult to describe and exhibit randomness to a certain extent [23]. Moreover, they require a large number of training samples and need to reselect samples for different data types [23]–[25]. Fmask algorithm was developed to extract clouds in Sentinel 2 and Landsat images. This algorithm works well for all three scenarios (Landsats 4–7, Sentinel 2, and Landsat 8) [7], [26]. However, due to the different spectral bands that each scenario uses, the accuracies of the Fmask results are quite different. The Fmask results from Sentinel 2 images are much more accurate than the Fmask results from Landsat 4–7 images [26]. However, Fmask may fail to extract clouds in images that have heterogeneous surface reflectances because it uses a scene-based threshold and applies the same threshold to all pixels in the image [27]. Therefore, achieving high precision remains challenging.

To tackle this problem, in this paper, a cloud extraction scheme is proposed that can effectively solve the problem of the confusion of clouds and high brightness reflectivity cover caused by the similar spectral characteristics in traditional cloud extraction methods. The main contributions of this paper are summarized as follows.

1. We propose a framework based on principal component analysis (PCA), fractal summation model, Anselin Local Moran's I index, and anisotropy for cloud extraction from Landsat-8 OLI images with high brightness reflectivity.

2. PCA and a fractal summation model are applied together to extract clouds associated with anomalies. This approach can separate objects that are easily confused due to their similar spectral characteristics and obtain an accurate and reliable threshold.

3. Anselin Local Moran's I index is used to determine the cluster and outlier states of the spatial distribution and eliminate false anomalies based on the spatial information.

4. Anisotropy is introduced to reduce the misjudgment of thick snow and improve the universality and accuracy of the proposed cloud extraction method.

Compared with two existing effective methods, the novel cloud extraction scheme proposed in this article has a better effect on the images with high brightness reflectivity.

II. METHODS

A. PRINCIPAL COMPONENT ANALYSIS (PCA)

PCA, which is widely used in remote sensing image processing, is a mathematical technique for reducing the dimensionality of a data set [28]. Because digital remote sensing images are numeric, their dimensionality can be reduced using this technique. In multiband remote sensing images, the bands are the original variables. Some of the original bands may be highly correlated, and to save data storage space and computing time, such bands could be combined into new, less correlated images by PCA [29]. PCA determines the eigenvectors of a variance–covariance or a correlation matrix, and the resulting component images are often more interpretable than their original counterparts. Thus, certain objects of interest can be delineated [30]. PCA aims to put the maximum possible information in the first principal component (PC1), maximizes the remaining information in the second

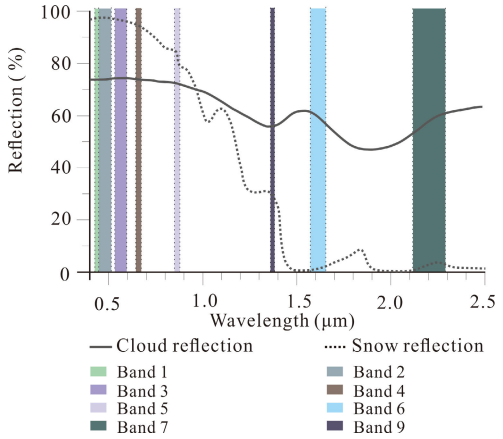

FIGURE 1. Reflection spectra of clouds and snow [31], [32].

component and so on. The first principal component accounts for the most possible ground object information in the remote sensing data set. The next principal component is calculated in the same way with the condition that it is uncorrelated with the first principal component and that it accounts for the second most information.

The spectral curves of snow and clouds are similar in shape and have high reflectivity in Band 3 (visible band), but their spectral curves are then different in Band 6 (1.560-1.660 μm) and Band 9 (1.360-1.390 μm). The reflectivity of clouds remains high, whereas the reflectivity of ice/snow decreases dramatically, as shown in Fig. 1 [12]. The three bands with the largest difference in their reflectivity between snow and clouds are selected, which will facilitate their separation [33].

B. CLOUD EXTRACTION BASED ON THE FRACTAL SUMMATION MODEL

The fractal summation model was originally designed to separate the geochemical anomalies associated with ore deposits [34]. Here, we apply this model to cloud extraction of remote sensing images. A remotely sensed image is composed of an array of pixels, and each pixel is marked by a digital number (DN) value; thus, this scheme can be used to provide a visual representation of the variance of an image based on the pixel values and pixel value frequency distribution, or even the spatiotemporal and geometrical properties of image patterns [35]. The fractal model that is used in this study is known as the fractal summation method, and its basic calculation formula can be derived as follows:

$$N(r) = C \cdot r^{-D_n} \tag{1}$$

where r is the characteristic linear measurement. Here, r stands for the images' pixel values from small to large, Dn (n = 1, 2, 3, 4...) is the fractal dimension, and C is a proportionality constant. Each dimension corresponds to one scale-free (linear) segment and reflects the number of pixels or the summation of the pixel values that are equal to and greater than the corresponding r [36]. Taking the logarithms of the above formula, we obtain the following:

$$\log N(r) = -D_n \log(r) + \log C \tag{2}$$

A plot of log N(r) versus log (r) can produce several straight lines (at least two) with different slopes: D1, 2, 3...For a single straight line, by virtue of the linear least-square regression, the data set (N (ri), ri) (i=1, 2, ...N) can be fit as a straight line, and its corresponding slope is noted as D. For two straight line segments that are fit by the least squares with the two slopes D1 and D2, the dividing point is determined by the optimum least-square regression method as follows, which is the residual sum of squares (RSS). It is defined as follows:

$$RSS = \sum_{i=1}^{i_0} [\lg N(ri) + D1 \lg ri - \lg C1]^2 + \sum_{i=i_0+1}^{N} [\lg N(r_i) + D_2 \lg r_i - \lg C_2]^2 \rightarrow Min \tag{3}$$

The separation point between different Dn is denoted as Tn (n = 1, 2, 3, 4...), i.e., the anomaly threshold. In a similar fashion, the slopes of several scale-invariant segments, as well as the thresholds (Tn, n = 1, 2, 3 ...) between them, can be accurately determined. i_0 represents each pixel value that is traversed from small to large.

The details and the MATLAB implementation of this scheme can be found in the references within Zhao *et al.* [37].

C. ANSELIN LOCAL MORAN'S I

Anselin Local Moran's I measures the degree of spatial autocorrelation at a specific location [38]–[40]. Given a set of features and an analysis field, the Anselin Local Moran's I index identifies the spatial clusters of features with high or low values. The tool also identifies spatial outliers. To do this, it calculates a Local Moran's I value for each statistically significant feature [41].

The Local Moran's I statistic of spatial association is calculated as follows:

$$I_i = \frac{x_i - \overline{X}}{S_i^2} \sum_{j=1, j\neq i}^{n} w_{i,j} \left(x_j - \overline{X}\right) \tag{4}$$

where x_i is an attribute for feature i, $\overline{X}$ is the mean of the corresponding attribute, $w_{i,j}$ is the spatial weight between feature i and j,

$$S_i^2 = \frac{\sum_{j=1, j\neq i}^{n} \left(x_j - \overline{X}\right)^2}{n-1} \tag{5}$$

and n is the total number of features.

D. ANISOTROPIC ANALYSIS

The anisotropy and pixel value are two basic properties that make a spatial group inseparable. For the sake of simplicity,

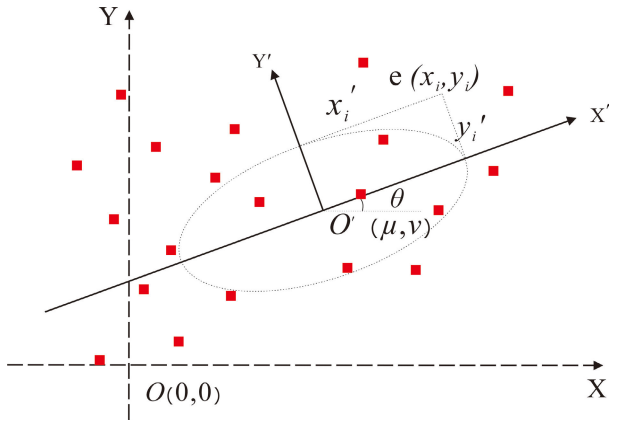

FIGURE 2. Plot of a standard deviational ellipse.

we use standard deviation ellipses to study the anisotropy. A common way of measuring the trend for a set of points or areas is to calculate the respective standard distances in the x and y directions. These two measures define the axes of an ellipse encompassing the distribution of features. The ellipse is referred to as the standard deviational ellipse because the method calculates the standard deviation of the x coordinates and y coordinates from the mean center to define the axes of the ellipse. The ellipse allows you to see if the distribution of features is elongated and hence has a particular orientation. While you can get a sense of the orientation by drawing the features on a map, calculating the standard deviational ellipse makes the trend clear. A standard deviational ellipse delineates the geographical distribution trend by summarizing both the dispersion and orientation of the observed samples [42], [43]. Suppose a series of independent identically distributed samples (x_i, y_i), where i = 1,...,n are drawn in a standard planar coordinate system (XOY), as illustrated in Fig. 2. If all observed sample points are then transformed into a new coordinate system (X'O'Y'), the origin of the new coordinate system is the average midpoint (u, v) of all point sets, as shown in Fig. 2.

The values of u and v represent the average X value and Y value, respectively, of all points in the original coordinates, and the relevant equations are given as follows:

$$u = \frac{\sum_{i=1}^{n} x_i}{n}, \quad v = \frac{\sum_{i=1}^{n} y_i}{n} \tag{6}$$

The standard deviation distance to the X-axis in the new coordinate system can be represented as follows:

$$\sigma_{y'} = \sqrt{\frac{\sum_{i=1}^{n} [(y_i - v)\cos\theta - (x_i - \mu)\sin\theta]^2}{n}} \tag{7}$$

By defining $\bar{y}_i = y_i - v$ and $\bar{x}_i = x_i - \mu$ and substituting them into equation (7), the equation of $\sigma_{y'}$ can be expressed as follows:

$$\sigma_{y'} = \sqrt{\frac{\sum_{i=1}^{n} \bar{y}_i^2 \cos^2\theta - 2\sum_{i=1}^{n} \bar{x}_i\bar{y}_i \sin\theta\cos\theta + \sum_{i=1}^{n} \bar{x}_i \sin^2\theta}{n}} \tag{8}$$

Similarly to $\sigma_{x'}$, two standard deviation distances are obtained in which the maximal standard deviation distance $\sigma_{x'}$ is the length of the long axis of the ellipse, and the minimal standard deviation distance σ_y' is the short axis of the ellipse. The angle of rotation is defined as follows:

$$\begin{aligned} \tan\theta &= \frac{A \pm B}{C} \\ A &= (\sum_{i=1}^{n} \bar{x}_i - \sum_{i=1}^{n} \bar{y}_i) \\ B &= \sqrt{(\sum_{i=1}^{n} \bar{x}_i - \sum_{i=1}^{n} \bar{y}_i)^2 + 4(\sum_{i=1}^{n} \bar{x}_i\bar{y}_i)^2} \\ C &= 2\sum_{i=1}^{n} \bar{x}_i\bar{y}_i \end{aligned} \tag{9}$$

θ is the rotation angle of the coordinate system, that is, the directional orientation of the point set. Along the stretching direction of the thicker clouds, some thinner clouds that are difficult to extract can thus be included in the anomaly patches using an appropriate buffering zone [44].

III. EXPERIMENTAL ANALYSIS

A. REMOTE SENSING DATA

The selected data are Landsat 8 OLI imagery. The scene image was quite typical, showing thick and thin clouds as well as snow cover; we also analyzed images with higher cloud coverage and analyzed different regions to verify the applicability of the method proposed here. As illustrated in Fig. 3, the original image was cut into the spatial scope of the study area.

B. CLOUD EXTRACTION BASED ON THE PIXEL VALUES

1) PRINCIPAL COMPONENT ANALYSIS (PCA)

In this study, Bands 3, 6, and 9, which contain some diagnostic absorption and reflection features of clouds and snow (Fig. 1), were selected for PCA. The reflectivity difference between the snow and clouds is denoted as the highest difference among the three bands, which is beneficial for separating them. The output images of the PCA are shown in Fig. 4. The highlighted spectral responses related to specific object information in PC1 (red frame in Fig. 4a) do not correspond to clouds; rather, they indicate ice and snow. The highlighted spectral responses related to specific object information in PC2 and PC3 correspond to clouds (clouds appear bright and are associated with high PC value). In PC3, the brightness of the clouds is evident, which is exactly the opposite of the case of PC1.

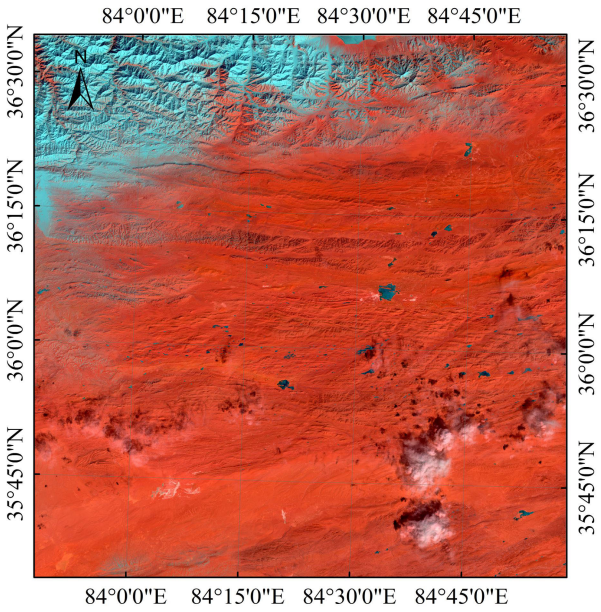

FIGURE 3. Landsat 8 satellite image of the study area (The false color composite helps the reader visually differentiate between snow/ice and clouds. Bands 7, 2, and 1 are represented by red, green, and blue, respectively.)

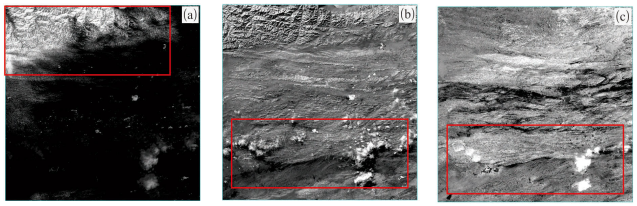

FIGURE 4. Output images of the PCA. Red frames represent highlighting spectral responses. (a) PC1; (b) PC2; (C) PC3.

Quantitatively, Table 1 records the statistical output of the PCA. It is evident that PC1 reflects the presence of clouds because it is positive in Band 3 and negative in Band 6 and Band 9. This result is consistent with cloud absorption and reflection characteristics, although PC1 indicates the presence of clouds and considerable snow anomalies. Thus, it is difficult to distinguish between clouds, snow, and even desert areas. The results of PC2 are also consistent with those of cloud features because the reflectivity of the clouds in Band 3 is lower than the corresponding values of ice and snow. Moreover, the eigenvalues are negative, thus satisfying this feature. Clouds have higher reflectivity than ice and snow in Band 9, as shown in Fig. 1. PC3 is positive in Band 9 and captures this feature.

In conclusion, although PC1 can reflect the existence of clouds, it also highlights the existence of most ice and snow, which will lead to more false anomalies. PC2 and PC3 can reflect many spectral differences between clouds and snow, making them more useful for cloud recognition. In summary, PC2 and PC3 are the most effective choices for subsequent cloud extraction analysis.

TABLE 1. Eigenvalues for the selective PCA of Landsat 8 bands.

	Band 3	Band 6	Band 9
PC1	0.85	-0.53	-0.02
PC2	-0.71	-0.62	-0.66
PC3	-0.34	-0.57	0.75

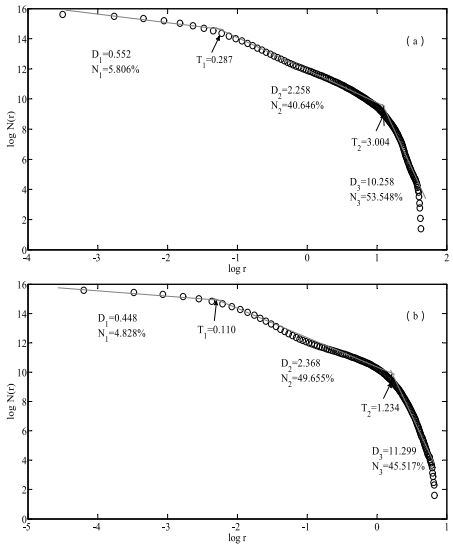

FIGURE 5. The log r versus log N(r) fractal schema of (a) PC2 and (b) PC3.

2) CLOUD EXTRACTION BASED ON THE FRACTAL SUMMATION MODEL

Each of the scaleless ranges approximately corresponds to a ground object [45]. The nonscaling interval in Fig. 5 corresponds to approximately one ground target. As seen in Fig. 5, according to visual interpretation and the PC value characteristics, areas with the pixel values lager than T2 in Fig. 5 are representative of thick clouds; areas between T1 and T2 mainly represent thin clouds. The nonscaling interval also includes many false anomalies related to snow and ice.

When a cloud is extracted by the fractal summation model, the clouds and snow of different spatial distributions are classified into the same fractal (scaleless) range. This suggests that the extraction of certain anomalies cannot be achieved using pixel values alone. To address this problem, we explore the spatial analysis of anomalous point patterns.

C. SPATIAL ANALYSIS OF THE ANOMALIES

1) SPATIAL INTERSECT

Pixel values cannot be used exclusively to distinguish ground objects completely because false anomalies share similar spectral features with authentic anomalies, and spatial information is also necessary [46], [47]. The spatial intersect can be used to eliminate most of false anomalies and retain the authentic anomalies that shared by both, where the anomalies that are preserved have two notable features. The first feature is the degree of spatial clustering and the other is

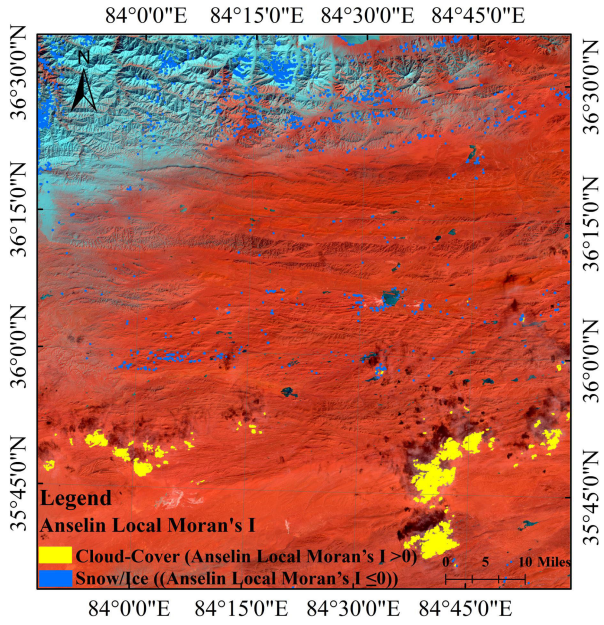

FIGURE 6. The output image of the Anselin local Moran's I index.

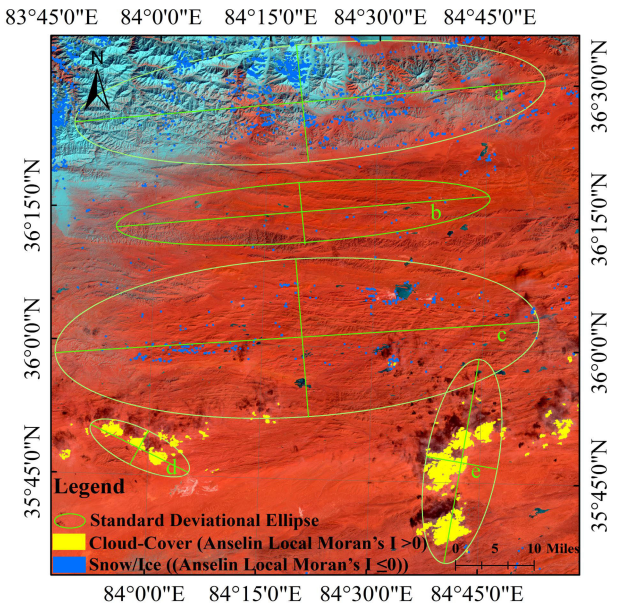

FIGURE 7. Schema of the standard deviation ellipses of the study area.

the directionality. A quantitative description of these two characteristics benefits the identification process.

2) ANSELIN LOCAL MORAN'S I

Here, Anselin Local Moran's I is used to exclude the false anomalies. The spatial cluster and outlier levels of snow/ice and clouds can be obtained by Anselin Local Moran's I using ArcGIS 10.2 software. The Moran's I was computed for each site and monitoring period to evaluate whether the distributional pattern was clustered, dispersed or random. Moran's I values range from $+1$ (strong positive autocorrelation) to -1 (strong negative autocorrelation) with a value of 0 indicating a random distribution [48]. Therefore, regions with positive values represent clustering. Anselin Local Moran's I reflects the location of high or low clustering values.

The results of the clump operation, which are calculated after Anselin Local Moran's I, are shown in Fig. 6. This operation enables the original clustering or dispersion tendency to be further enhanced. The two patches representing clouds and snow/ice can be separated using Anselin Local Moran's I. In general, the values of snow/ice are much lower than those of clouds, even when clouds are thin. This confirms our hypothesis that cloud cover is clustered and snow/ice is not.

However, we cannot exclude the possibility that some false anomalies such as large-sized glaciers and snow-capped mountainous areas could be mistaken as clouds using this method. Hence, the anisotropy of the anomalies must be considered.

3) ANISOTROPIC ANALYSIS

Standard deviation ellipses are used to study the anisotropy. The standard deviation ellipse of ice and snow is greatly affected by the topographic trend [42], [49]. For example, topography controls the elevation, wind direction, climate and other factors. High-altitude areas are covered with snow all year round while the shady sides of mountains are more likely to develop frozen soil, snow, glaciers and other features than the sunny side. According to the geometric shape of the standard deviation ellipse, this type of terrain can be distinguished. The distribution of snow/ice has a strong orientation and is obviously controlled by the trend of the high-altitude mountains or terrain. Clouds have no such restrictions. The standard deviation ellipses of all anomalous groups are drawn by ArcGIS, and the true and false anomalies (clouds or snow/ice) can be distinguished by comparing their rotation angles with the direction of the mountain strike and the extension of false anomalies. This allows the false anomalies of ice and snow to be eliminated and misjudgments to be reduced. Another advantage of the standard deviation ellipse is that it can create a buffer, which can identify the residual thin clouds according to the wind direction, and establish a weighted buffer at the boundary of the main extension direction of the extracted clouds, which greatly improves the accuracy of cloud extraction and improves the universality of the cloud extraction method. The standard deviation ellipses that can quantitatively reflect the anisotropy of the spatial point patterns are plotted in Fig. 7; the ellipses were automatically generated and the results of the previous step automatically grouped based on the ArcGIS 10.2 software platform.

Following the anisotropic analysis states, the rotation angles of d and e (clouds), which are characterized by the NS-trending long-axis direction, obviously show the opposite tendency of a, b, and c (ice/snow). This indicates that the spatial distribution pattern of snow/ice is different, and clouds tend to be dispersed whereas cloud cover is integrated. We applied a 100-m buffer along the main direction of the

TABLE 2. Data information of the standard deviation ellipses.

Number	Rotation angle (°)	Long axis length (m)	Short axis length (m)
a	5.61	40536.95	9361.05
b	4.37	32497.18	4878.12
c	3.82	42833.50	12345.19
d	334.62	8741.66	3064.10
e	79.09	16549.30	5748.61

stretch of the extracted clouds that were attached to the patches of thick clouds so that we could incorporate some thinner clouds that were not previously extracted. Clouds cannot be found using pixel values only or clustering characteristics, thus confirming the advantage of employing point process spatial analysis.

IV. RESULTS AND DISCUSSION

When selecting the cloud-sensitive principal components (namely, PC2 and PC3), the fractal summation model produced several errors. The extracted features were mainly spectral characteristics similar to those of clouds, such as snow or desert regions, indicating that pixel values alone cannot identify cloud regions. To account for this, we proposed a spatial point analysis method, which included Anselin Local Moran's I analysis and anisotropic analysis. Anselin Local Moran's I index avoided the interference from the fact that false anomalies share some similar spectral characteristics with clouds by using the degree of spatial clustering to eliminate false anomalies. Anisotropic analysis was able to eliminate the false anomalies that were not distributed along the main orientation, further reducing the number of false anomalies.

This method can be used to extract clouds with high precision in difficult areas with high-reflectivity snow and ice. Quantitatively, the results of the cloud extraction using the extracted cloud-covered data indicated an overall accuracy exceeding 96%. We selected eight Landsat 8 scenes with snow/ice and high-reflectance ground cover to test this method. Five regions of interest were selected, which are shown in the red frames. Cloud extraction in the absence of snow/ice was also found to be highly accurate (see the top scene in the data set).

Here, the yellow-colored areas represent clouds, while the black-colored areas represent features other than clouds. Visually, this method can effectively solve the problem that snow is often mistakenly classified as clouds. Quantitatively, to verify the effectiveness of this method, we compare it with ANN and Fmask approaches, which are two algorithms with good cloud extraction results [15]–[17], [26], [27]. Fig. 9 shows the five regions of interest and the associated cloud extraction results. The first column in Fig. 9 is the enlarged view of the indicated detailed areas that are shown in the red frames, which cover various underlying

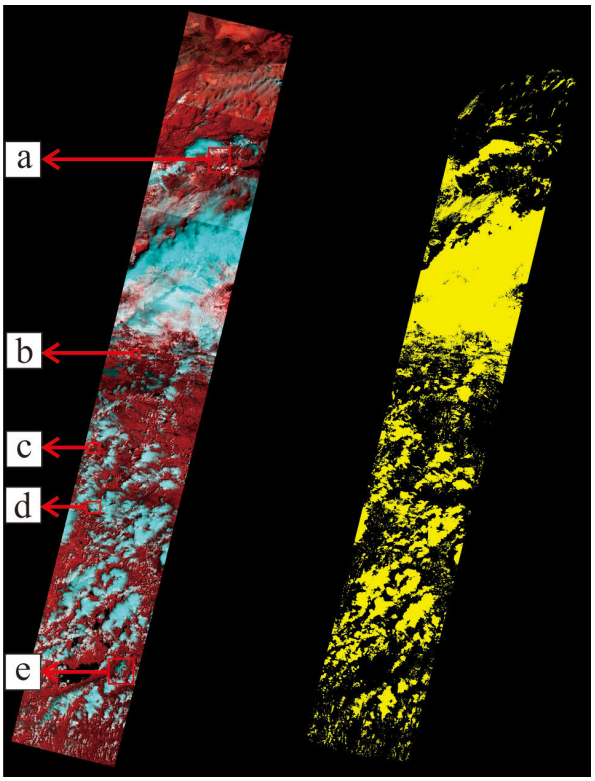

FIGURE 8. Proposed method results of eight Landsat 8 scenes. Five regions of interest were selected, and cloud masks are shown in yellow.

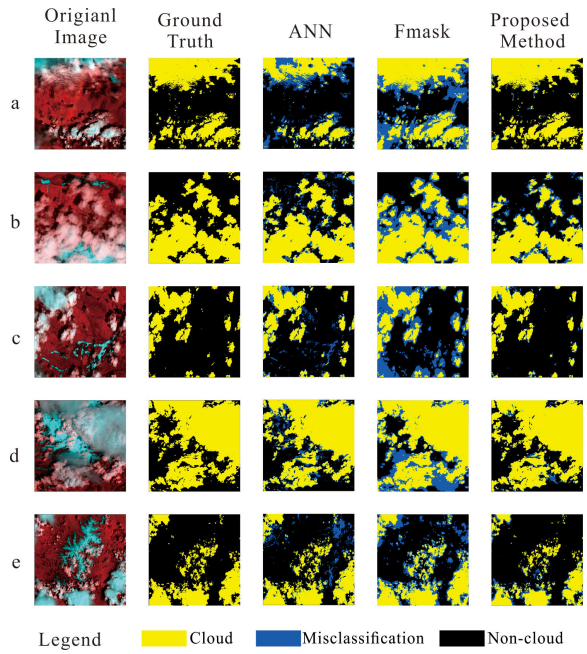

FIGURE 9. Comparison of the proposed method against the ANN and Fmask approaches using the five regions of interest in Fig. 8.

surface environments containing a bright background, mountains, and snow. The second column is the ground truth image; ground truths of cloud areas were manually extracted. Columns 3-5 are the cloud extraction results using the ANN,

TABLE 3. Precision, recall, and accuracy of the regions of interest.

		Accuracy	Recall	Precision
ANN	a	86.72%	80.88%	85.03%
	b	93.73%	91.42%	93.85%
	c	94.52%	84.06%	90.79%
	d	94.48%	93.40%	96.85%
	e	93.19%	76.45%	89.35%
Fmask	a	89.49%	98.57%	79.79%
	b	90.43%	98.47%	82.62%
	c	88.50%	97.59%	66.61%
	d	91.64%	99.01%	87.92%
	e	93.62%	97.79%	77.50%
Proposed Method	a	97.57%	95.88%	97.97%
	b	96.01%	93.59%	97.04%
	c	97.25%	92.01%	95.55%
	d	96.84%	96.37%	98.08%
	e	97.12%	90.60%	95.36%

Fmask, and proposed method. We applied the ANN and Fmask approaches in ENVI 5.4 software.

From Fig. 9, it is obvious that all methods can extract most of the clouds; but for the snow and high-reflectivity regions, our proposed method can achieve more accurate results because our method captures three broad cloud characteristics: the pixel value, spatial cluster and outliers, and anisotropy, and the algorithm more easily addresses the problem that snow and high-reflectivity ground cover are often misclassified as clouds.

The qualitative evaluation was an important aspect of the development of the algorithm. Table 3 quantifies the results of the above cloud extraction figure. In this paper, the accuracy, recall and precision are defined as follows:

$$\text{Accuracy} = \frac{(TP + TN)}{(TP + TN + FP + FN)} \tag{10}$$

$$\text{Recall} = \frac{TP}{(TP + FN)} \tag{11}$$

$$\text{Precision} = \frac{TP}{(TP + FP)} \tag{12}$$

where TP is the number of true positives (i.e., correctly classified cloud pixels), TN represents the number of true negatives (i.e., correctly classified clear pixels), FP is the number of false positives (i.e., clear pixels classified as cloud pixels) and FN is the number of false negatives (i.e., cloudy pixels classified as clear pixels) [50]. These indexes range from 0 to 100%, where the maximum value represents the best fit.

To quantitatively measure the detection accuracy using the proposed algorithm, we compared the precision, recall, and accuracy against the ANN and Fmask methods. The statistical cloud extraction results are listed in Table 3. The accuracy is the fraction of pixels that are correctly classified, the precision is the fraction of pixels that are correctly classified as clouds, and the recall is the fraction of cloudy pixels that are correctly classified with respect to the total number of cloud pixels. It can be seen that the method proposed in this paper yields the best accuracy and precision, although its recall is slightly lower than that of the Fmask approach. Fmask can obtain slightly more true positives; however, its false positions are far more than the other two approaches, with the most misclassification. This indicates that its accuracy and precision are low.

Although the recall of the proposed method is slightly lower, the basic requirement of highly accurate cloud extraction is not affected. The overall accuracy of the proposed approach remains above 96%, and the recall rate remains above 90%. Overall, the proposed method obtains a precision of more than 95%, and it performs well in terms of the recognition of clouds in areas with very bright land surfaces.

V. CONCLUSION

The scheme proposed in this paper used pixel values, Anselin Local Moran's I index, and anisotropic analysis to extract clouds. This method could solve the problem that snow was often misclassified as clouds in traditional extraction methods. In addition, the method eliminated the salt and pepper noise generated by bright surfaces and greatly improved the accuracy of cloud extraction. Therefore, this method could be generalized because it captured three broad cloud characteristics: the pixel value, the spatial cluster and outliers, and the anisotropy.

(1) We selected a larger area with snow/ice and high-reflectance ground cover to verify the proposed method. In addition, this method also achieved ideal cloud extraction results in areas without snow and ice cover. Therefore, we draw the following conclusions: PCA could separate objects that are easily confused due to their similar spectral characteristics, and different principal components show many spectral differences between clouds and snow, making them more useful for cloud recognition.

(2) The fractal summation model could obtain an accurate and reliable threshold, but pixel values couldn't be used to completely distinguish features because false anomalies share some spectral features with authentic anomalies. Therefore, another diagnostic characteristic was adopted, i.e., spatial information.

(3) Anselin Local Moran's I analysis was used to determine the cluster and outlier states of spatial distribution. Clouds are clustered, while the salt and pepper noise generated by snow/ice and high-reflectivity ground cover is dispersed. Therefore, most of the snow/ice and high-reflectance ground cover could be eliminated by the spatial distribution information of clouds and erroneous anomalies.

(4) We used standard deviation ellipses to study the anisotropy. The directional information of a standard deviation ellipse can reduce the misjudgment of thick snow that does not have a discrete distribution all year round and eliminate false anomalies according to the direction. In addition, another advantage of the anisotropy is the buffer. We used the above method to set a weighted buffer at the boundary of the main extension direction of the extracted cloud, which greatly improves the cloud extraction accuracy and improves the universality of cloud extraction methods. The introduction of anisotropy analysis could eliminate false anomalies that do not follow a dispersed distribution and greatly improve the cloud extraction accuracy.

ACKNOWLEDGMENT

The authors would like to thank the editors and anonymous reviewers for their insightful comments and suggestions, which helped to significantly improve this paper.

REFERENCES

[1] Y. Li, R. Yu, Y. Xu, and X. Zhang, "Spatial distribution and seasonal variation of cloud over china based on ISCCP data and surface observations," *J. Meteorol. Soc. Jpn.*, vol. 82, no. 2, pp. 761–773, 2004.

[2] R. A. Schowengerdt, *Remote Sensing: Models and Methods for Image Processing*, 2nd ed. Burlington, VT, USA: Elsevier, 2012.

[3] J. A. Richards, *Remote Sensing Digital Image Analysis*. Berlin, Germany: Springer, 1986.

[4] H. Shen, H. Li, Y. Qian, L. Zhang, and Q. Yuan, "An effective thin cloud removal procedure for visible remote sensing images," *ISPRS J. Photogramm. Remote Sens.*, vol. 96, pp. 224–235, Oct. 2014.

[5] X. Song, Z. Liu, and Y. Zhao, "Cloud detection and analysis of MODIS image," in *Proc. Int. Geosci. Remote Sens. Symp. (IGARSS)*, 2004.

[6] S. Platnick, M. King, S. Ackerman, W. Menzel, B. Baum, J. Riedi, and R. Frey, "The MODIS cloud products: Algorithms and examples from Terra," *IEEE Trans. Geosci. Remote Sens.*, vol. 41, no. 2, pp. 459–473, Feb. 2003.

[7] Z. Zhu and C. E. Woodcock, "Object-based cloud and cloud shadow detection in Landsat imagery," *Remote Sens. Environ.*, vol. 118, pp. 83–94, Mar. 2012.

[8] H. Choi, "Cloud detection in Landsat imagery of ice sheets using shadow matching technique and automatic normalized difference snow index threshold value decision," *Remote Sens. Environ.*, vol. 91, no. 2, pp. 237–242, May 2004.

[9] G. A. Riggs and D. K. Hall, "Reduction of cloud obscuration in the MODIS snow data product," in *Proc. 59th Eastern Snow Conf.*, Jun. 2002, vol. 5, no. 7, pp. 1–8.

[10] Z. Zhu and C. E. Woodcock, "Automated cloud, cloud shadow, and snow detection in multitemporal Landsat data: An algorithm designed specifically for monitoring land cover change," *Remote Sens. Environ.*, vol. 152, pp. 217–234, Sep. 2014.

[11] S. A. Ackerman, K. I. Strabala, W. P. Menzel, R. A. Frey, C. C. Moeller, and L. E. Gumley, "Discriminating clear sky from clouds with MODIS," *J. Geophys. Res. Atmos.*, vol. 103, no. D24, pp. 32141–32157, Dec. 1998.

[12] R. G. Crane and M. R. Anderson, "Satellite discrimination of snow/cloud surfaces," *Int. J. Remote Sens.*, vol. 5, no. 1, pp. 213–223, Jan. 1984.

[13] V. Salomonson and I. Appel, "Estimating fractional snow cover from MODIS using the normalized difference snow index," *Remote Sens. Environ.*, vol. 89, no. 3, pp. 351–360, Feb. 2004.

[14] J. W. Homan, C. H. Luce, J. P. Mcnamara, and N. F. Glenn, "Improvement of distributed snowmelt energy balance modeling with MODIS-based NDSI-derived fractional snow-covered area data," *Hydrol. Process.*, vol. 25, no. 4, pp. 650–660, Feb. 2011.

[15] D. E. Rumelhart, G. E. Hinton, and R. J. Williams, "Learning Internal Representations by Error Propagation," in *Readings in Cognitive Science*. Amsterdam, The Netherlands: Elsevier, 1988, pp. 399–421.

[16] R. R. Jensen, P. J. Hardin, and G. Yu, "Artificial neural networks and remote sensing," *Geogr. Compass*, vol. 3, no. 2, pp. 630–646, 2009.

[17] J. F. Mas and J. J. Flores, "The application of artificial neural networks to the analysis of remotely sensed data," *Int. J. Remote Sens.*, vol. 29, no. 3, pp. 617–663, Feb. 2008.

[18] T. Bai, D. Li, K. Sun, Y. Chen, and W. Li, "Cloud detection for high–resolution satellite imagery using machine learning and multi–feature fusion," *Remote Sens.*, vol. 8, no. 9, p. 715, Aug. 2016.

[19] B. Han, L. Kang, and H. Song, "A fast cloud detection approach by integration of image segmentation and support vector machine," in *Advances in Neural Networks—ISNN* (Lecture Notes in Computer Science: Lecture Notes in Artificial Intelligence and Lecture Notes in Bioinformatics), 2006.

[20] M. Xu, X. Jia, and M. Pickering, "Automatic cloud removal for Landsat 8 OLI images using cirrus band," in *Proc. IEEE Geosci. Remote Sens. Symp.*, Jul. 2014, pp. 2511–2514.

[21] G. Chen and E. Dongchen, "Support vector machines for cloud detection over ice-snow areas," *Geo-Spatial Inf. Sci.*, vol. 10, no. 2, pp. 117–120, Jan. 2007.

[22] N. T. Y. Shan Zheng and Z. S. Wang, "High-speed and high-accuracy algorithm for cloud detection and its application," (in Chinese), *J. Remote Sens.*, vol. 13, no. 6, pp. 1138–1155, 2009.

[23] H. Wu, X. Hu, H. Cao, and J. Sun, "Shape feature-assisted discrimination of cloud and snow in GF–1 spectral images of mountainous areas," *Remote Sens. Lett.*, vol. 9, no. 11, pp. 1020–1029, Nov. 2018.

[24] C. Latry, C. Panem, and P. Dejean, "Cloud detection with SVM technique," in *Proc. IEEE Int. Geosci. Remote Sens. Symp.*, Jul. 2007, pp. 448–451.

[25] G. Chen and E. D. Chen, "Cloud detection based on texture analysis and SVM over ice-snow covered area," *Geomatics Inf. Sci. Wuhan Univ.*, vol. 31, no. 5, pp. 403–406, 2006.

[26] Z. Zhu, S. Wang, and C. E. Woodcock, "Improvement and expansion of the Fmask algorithm: Cloud, cloud shadow, and snow detection for Landsats 4–7, 8, and Sentinel 2 images," *Remote Sens. Environ.*, vol. 159, pp. 269–277, Mar. 2015.

[27] D. S. Candra, S. Phinn, and P. Scarth, "Cloud and cloud shadow masking using multi-temporal cloud masking algorithm in tropical environmental," *ISPRS-Int. Arch. Photogramm. Remote Sens. Spat. Inf. Sci.*, vol. XLI-B2, pp. 95–100, Jun. 2016.

[28] B. B. Jackson and B. Bund, *Multivariate Data Analysis: An Introduction*. Bingley, U.K.: MCB UP Ltd, 1983.

[29] C. Munyati, "Use of principal component analysis (PCA) of remote sensing images in wetland change detection on the Kafue Flats, Zambia," *Geocarto Int.*, vol. 19, no. 3, pp. 11–22, Sep. 2004.

[30] S. Jung and J. S. Marron, "PCA consistency in high dimension, low sample size context," *Ann. Statist.*, vol. 37, no. 6B, pp. 4104–4130, Dec. 2009.

[31] R. C. Allen, P. A. Durkee, and C. H. Wash, "Snow/cloud discrimination with multispectral satellite measurements," *J. Appl. Meteor.*, vol. 29, no. 10, pp. 994–1004, Oct. 1990.

[32] C. Dong, "Remote sensing, hydrological modeling and *in situ* observations in snow cover research: A review," *J. Hydrol.*, vol. 561, pp. 573–583, Jun. 2018.

[33] S. Y. Feng, N. Zhang, and J. Shen, "Method of cloud detection with hyperspectral remote sensing image based on the reflective characteristics," (in Chinese), *Chin. Opt.*, vol. 8, no. 2, pp. 198–204, 2015.

[34] Q. Cheng, "The perimeter-area fractal model and its application to geology," *Math. Geol.*, vol. 27, no. 1, pp. 69–82, Jan. 1995.

[35] C. Brekke and A. H. Solberg, "Oil spill detection by satellite remote sensing," *Remote Sens. Environ.*, vol. 95, no. 1, pp. 1–13, Mar. 2005.

[36] T. Blenkinsop, "Scaling Laws for the distribution of gold, geothermal, and gas resources," *Pure Appl. Geophys.*, vol. 172, no. 7, pp. 2045–2056, Jul. 2015.

[37] B. Zhao, L. Yu, J. T. Qiu, and C. L. Shi, "Internal structural analysis of geochemical anomaly based on the content arrangement method: A case study of copper stream sediment survey in northwestern Zhejiang Province," (in Chinese), *Geophys. Geochem. Explor.*, vol. 39, no. 2, pp. 297–305, 2015.

[38] L. Anselin, "Local indicators of spatial association–LISA," *Geograph. Anal.*, vol. 27, no. 2, pp. 93–115, Sep. 2010.

[39] L. Anselin, "The Moran scatterplot as an ESDA tool to assess local instability in spatial association," in *Spatial Analytical*. London, U.K.: Routledge, 2019, pp. 111–126.

[40] L. Anselin, "Exploring spatial data with GeoDa: A workbook," Dept. Geography, Spatial Anal. Lab., Univ. Illinois Urbana-Champaign, Urbana, IL, USA, 2005. [Online]. Available: https://www.sal.uiuc.edu/stuff/stuff-sum/pdf/geodaworkbook.pdf

[41] *ArcGIS Desktop. Release 10.1*, ESRI, Environ. Syst. Res. Inst., Redlands, CA, USA, 2012.
[42] J. Gong, "Clarifying the standard deviational ellipse," *Geograph. Anal.*, vol. 34, no. 2, pp. 155–167, Apr. 2002.
[43] W. Baojun, S. Bin, and H. I. Inyang, "GIS-based quantitative analysis of orientation anisotropy of contaminant barrier particles using standard deviational ellipse," *Soil Sediment Contamination, Int. J.*, vol. 17, no. 4, pp. 437–447, Jun. 2008.
[44] T. Eryando, D. Susanna, D. Pratiwi, and F. Nugraha, "Standard Deviational Ellipse (SDE) models for malaria surveillance, case study: Sukabumi district-Indonesia, in 2012," *Malaria J.*, vol. 11, no. 1, p. P130, 2012.
[45] L. Han, B. Zhao, J.-J. Wu, S.-Y. Zhang, J. Pilz, and F. Yang, "An integrated approach for extraction of lithology information using the SPOT 6 imagery in a heavily Quaternary-covered region–North Baoji District of China," *Geol. J.*, vol. 53, pp. 352–363, Mar. 2018.
[46] L. Zhang, Q. Zhang, B. Du, X. Huang, Y. Y. Tang, and D. Tao, "Simultaneous spectral-spatial feature selection and extraction for hyperspectral images," *IEEE Trans. Cybern.*, vol. 48, no. 1, pp. 16–28, Jan. 2018.
[47] L. Zhang, L. Zhang, B. Du, J. You, and D. Tao, "Hyperspectral image unsupervised classification by robust manifold matrix factorization," *Inf. Sci.*, vol. 485, pp. 154–169, Jun. 2019.
[48] P. A. P. Moran, "The Interpretation of Statistical Maps," *J. Roy. Stat. Soc. B, Methodol.*, vol. 10, no. 2, pp. 243–251, Jul. 1948.
[49] P. H. Furfey, "A note on Lefever's 'standard deviational ellipse,"' *Amer. J. Sociol.*, vol. 33, no. 1, pp. 94–98, Jul. 1927.
[50] G. Ganci, A. Vicari, S. Bonfiglio, G. Gallo, and C. Del Negro, "A texton-based cloud detection algorithm for MSG-SEVIRI multispectral images," *Geomatics, Natural Hazards Risk*, vol. 2, no. 3, pp. 279–290, Sep. 2011.

TINGTING WU received the B.S. and M.S. degrees in remote sensing from Chang'an University, Xi'an, China, in 2014 and 2016, respectively, where she is currently pursuing the Ph.D. degree. Her research interest includes the cloud extraction in snow covered images and landslides interpretation in loess plateau areas.

LING HAN received the B.S. and M.S. degrees in remote sensing from Wuhan University, Wuhan, China, in 1991 and 1994, respectively, and the Ph.D. degree in remote sensing from Northwest University, Xi'an, China, in 2005. Her research interest includes the cloud extraction in snow covered images and landslides interpretation in loess plateau areas.